

Synthetic Kramers pair in phononic elastic plates and the imaging of helical edge states on a dislocation interface

Ting-Wei Liu and Fabio Semperlotti*

Ray W. Herrick Laboratories, School of Mechanical Engineering,
Purdue University, West Lafayette, Indiana 47907, USA.

(Dated: September 6, 2021)

In conventional theories, topological band properties are intrinsic characteristics of the bulk material and do not depend on the choice of the reference frame. In this scenario, the principle of bulk-edge correspondence can be used to predict the existence of edge states between topologically distinct materials. In this study, we propose and carefully examine a 2D elastic phononic plate with a Kekulé-distorted honeycomb pattern engraved on it. It is found that the pseudospin and the pseudospin-dependent Chern numbers are not invariant properties, and the \mathbb{Z}_2 number is no longer a sufficient indicator to examine the existence of the edge state. The distinctive pseudospin texture and the pseudomagnetic field are also revealed. Finally, we successfully devise and experimentally implement a synthetic Kramers pair helical edge state on a dislocation interface connecting two subdomains with bulk pattern identical up to a relative translation, and image the edge state.

I. INTRODUCTION

The study of topological states of matter has rapidly grown over the past few decades [1–3]. While the field of topological materials originated and had particular significance for the broader area of quantum mechanics, in recent years these works served as an inspiration to explore the existence of analog topological effects in classical waveguide systems [4–8]. These analog quantum mechanical mechanisms, on one side offered engineers a powerful route to design waveguides (either photonic, acoustic, or elastic) immune to backscattering generated by disorder or defects, on the other side were seen by physicists as ideal platforms to explore the effect of design parameters and to experimentally validate important fundamental concepts without the significant complexities imposed by the quantum scales. In other terms, the artificial photonic and phononic structures were treated as surrogate platforms to understand and develop the topological band theory and its practical implications.

To-date, several analog mechanisms have been explored and validated for classical waveguides. Initial attempts focused on the implementation and transposition of the concept of quantum Hall effect. However, these systems required breaking time reversal symmetry (TRS), which imposes significant practical complexities due to the need for either special magneto-optic and elastic materials, or for carefully controlled external input [9–16]. More recently, mechanisms analog to TRS-preserved quantum spin Hall effect (QSHE) [17–30] and quantum valley Hall effect [27, 31–37] were proposed. These systems could be built based on ordinary dielectric or linearly elastic materials, and only required the breaking of spatial symmetry, which was a considerably more practical approach. Among the TRS-preserved mechanisms, bosonic systems can leverage the same valley degree of freedom to realize an analog valley Hall effect. While the valley Hall effect and the associated backscattering immunity of the edge states count on large separation of states in momentum space, the classical analog to

QSH systems relies on decoupling of synthetic “pseudospin” states, which can potentially yield counter-propagating edge states that are close in momentum space while still being robust against backscattering.

Despite these successful initial implementations, the emulation of a quantum spin Hall topological insulator has proven to be a remarkably more complicated task. It is well known that the $\pm\frac{1}{2}$ -spin electronic systems exhibit the so-called Kramers pair (given that the time-reversal operator \mathcal{T} applied twice returns the initial state with additional negative sign, that is $\mathcal{T}^2 = -1$). It follows that that under TRS, every eigenstate has a partner with opposite momentum and spin and the same energy spectrum, that is $E(\mathbf{k}, \uparrow) = E(-\mathbf{k}, \downarrow)$. This condition guarantees the existence of gapless helical edge states that are time reversal counterparts of each other with opposite spins. While both photons and phonons are bosonic in nature, they do not possess the same intrinsic attributes. Researchers have proposed different ideas to synthesize properties analog to electron spins, often referred to as “pseudospins”. In phononic systems, examples include mixing of symmetric and antisymmetric Lamb modes in phononic waveguides [29, 30], and a “zone-folding” method [17–28] to attain a doubly degenerate Dirac cone at the center of the Brillouin zone that acts as a surrogate degree of freedom for electron spins. However, it was reported that phononic systems exploiting this mechanism typically gave rise to gapped edge states at zero momentum where the ω - \mathbf{k} dispersion curves of the counter-propagating edge states avoid intersecting [17–27]. These results showed that the edge states are not a Kramers pair and do not have a continuous spectrum across the bulk band gap. In addition, although the zone-folding approach is already widely adopted, previous studies concentrated on mapping the system back to the electronic counterpart but usually omitted explaining some discrepancies between the synthetic phononic pseudospins and the electron’s intrinsic spin, hence leaving behind some obscure points, such as the indeterminate pseudospin states and the seemingly indistinguishable topological phases.

In this paper, we propose an elastic analog of a topological insulator based on a 2D phononic waveguide designed according to a Kekulé distorted honeycomb pattern. The study uncovers interesting anomalous properties associated

* fsemperl@purdue.edu

with the generation of synthetic pseudospins and peculiar discrepancies with electron spins. These anomalous properties include indeterminate pseudospin-dependent Chern numbers and indistinguishable topological states, which are characteristic of the “zone-folding” approach and different from electronic QSH systems. Although the concepts of pseudospins and zone-folding have been discussed in the literature, a series of questions were left unexplored. The discrepancy between the classical “zone-folding system” and electronic QSH systems leads to consider the former as an “imperfect analogue” since proper “helical” edge state cannot be realized; in other terms, the counter-propagating edge states are found to be gapped and with strong coupling at $\mathbf{k} = 0$. However, as we face the discrepancy and investigate in depth its origin, we find a method to realize truly gapless helical edge states such that the counter-propagating edge states are fully decoupled, hence realizing a synthetic Kramers pair. In addition, we leverage the unique ambiguity of the topological state to achieve edge states along a *dislocation interface* connecting two sections of the same bulk lattice. This latter condition is not achievable in QSH systems that rely on determinate topological states.

This concept is also experimentally validated by directly imaging the response of the fabricated phononic lattice via laser vibrometry, and by extracting the spectrum of the edge state which matches well with the theoretical and numerical predictions. It is worth to highlight that these findings are particularly relevant from the practical perspective of waveguide design. In fact, not only this approach leads to robust and continuous gapless edge states, but it also allows exploiting the concept of dislocation that greatly simplifies the design. It is expected that the current design can be very well suited to achieve vibration and structure-borne noise control capabilities fully integrated in lightweight load bearing structures.

II. THE PHONONIC KEKULÉ LATTICE

The proposed phononic lattice consists in an aluminum thin waveguide (i.e. a thin plate) with a honeycomb-like groove pattern symmetrically engraved on both sides. The groove has a variable thickness according to an extended Kekulé distortion pattern. Fig. 1 (a) shows the benzene structure originally suggested by Kekulé which contains alternating double and single bonds. We adopt an extended version of the Kekulé distortion to define the groove depth of the honeycomb cell which allows three different “bonds” (i.e. the individual groove’s side of the cell) that can change their values (i.e. their depths) continuously, as shown in Fig. 1 (b). As shown in Fig. 2 (a), the phononic plate has thickness $b = 1/4$ inch (6.35 mm). Before incorporating the Kekulé distortion, the honeycomb groove has a constant depth h_0 and a lattice constant a_0 . The Kekulé distortion is then introduced by varying the groove depth according to the prescribed pattern. Three different depths $h_{1,2,3}$ are assigned at the midpoints of the hexagon edges, and the average depth $h_0 = (h_1 + h_2 + h_3)/3$ is assigned at the vertices of the hexagons joining the edges. The grooves are constructed by linearly connecting neighboring grooves, as schematically shown in the isometric view in Fig. 2 (b). Figure 2 (b) also

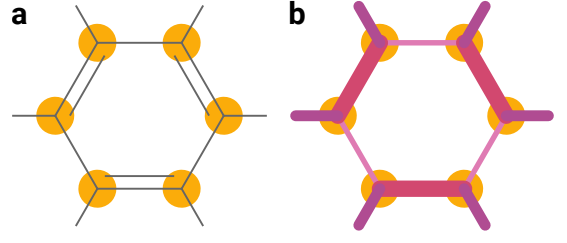


FIG. 1. (a) The benzene structure suggested by Kekulé which contains alternating double and single bonds. (b) The extended Kekulé distorted pattern used in our design. The bonds are replaced by the grooves (denoted in different colors) having different and continuously varying depth (illustrated by different line weight).

shows a top view of the Wigner-Seitz unit cell in the inset. Note that the Kekulé perturbation enlarges the primitive unit cell and the new lattice constant becomes $a = \sqrt{3}a_0$, as shown in Fig. 2 (a). Also, the lattice symmetry is degraded from D_6 to D_3 (or C_{6v} to C_{3v} in the context of 2D lattices). To facilitate the fabrication process, the groove width was chosen $D = 1/16$ inch, dictated by the diameter of the (ball-end) machining tool. Also the groove bottom was rounded so to match the actual slot cut by the tool. Implementing these few considerations allowed a substantial ease of fabrication via a computer numerical control (CNC) mill.

The three characteristic depths $h_{1,2,3}$ can be easily described by a set of parameters (h_0, δ, ϕ)

$$h_i = h_0 + \delta_i, \\ \delta_i = \delta \cos \left(\phi + (i-1) \frac{2\pi}{3} \right), \quad i = 1, 2, 3. \quad (1)$$

This parameter set $(h_0, \delta, \phi) \in \mathbb{R}^3$ can be considered as the natural coordinate system of the parametric space (h_1, h_2, h_3) governing the band structure. The first parameter, the average depth h_0 , affects the overall frequency shift of the phononic band structure, and plays no role in the topological transition. The second parameter δ controls the magnitude of the Kekulé distortion and therefore is related to the opening of the band gap. The parameter ϕ is the last free degree of freedom in the 3D parameter space and, will be shown later, is at the root of the peculiar behavior of the lattice. A graphical representation plotting the relation between (h_0, δ, ϕ) and (h_1, h_2, h_3) is shown in Fig. 2 (c). Note that given any real-number sequence (h_1, h_2, h_3) , one can always find an equivalent parameter set (h_0, δ, ϕ) that yields (h_1, h_2, h_3) . Given that the depth value must be positive, we can restrict $h_0 > 0$ and $-1 < \delta < 1$.

Due to the properties of the cosine function, we have $h_i|_{(\phi+\pi, \delta)} = h_i|_{(\phi, -\delta)}$, for all given (ϕ, δ) . Thus, the domain of (ϕ, δ) can be restricted to $[0, \pi) \times (-1, 1)$ and is still capable of generating all depth sequences (h_1, h_2, h_3) , as shown in Fig. 2 (d). Another interesting fact is that given any three sequences (h_1, h_2, h_3) , (h_2, h_3, h_1) and (h_3, h_1, h_2) composed of the same three numbers with the same cyclic permutation, they yield the same bulk lattice up to some rigid body translation (or rotation) of the lattice (or, equivalently, of the reference frame). For example, the permutation $(h_1, h_2, h_3) \rightarrow (h_3, h_1, h_2)$ is identical

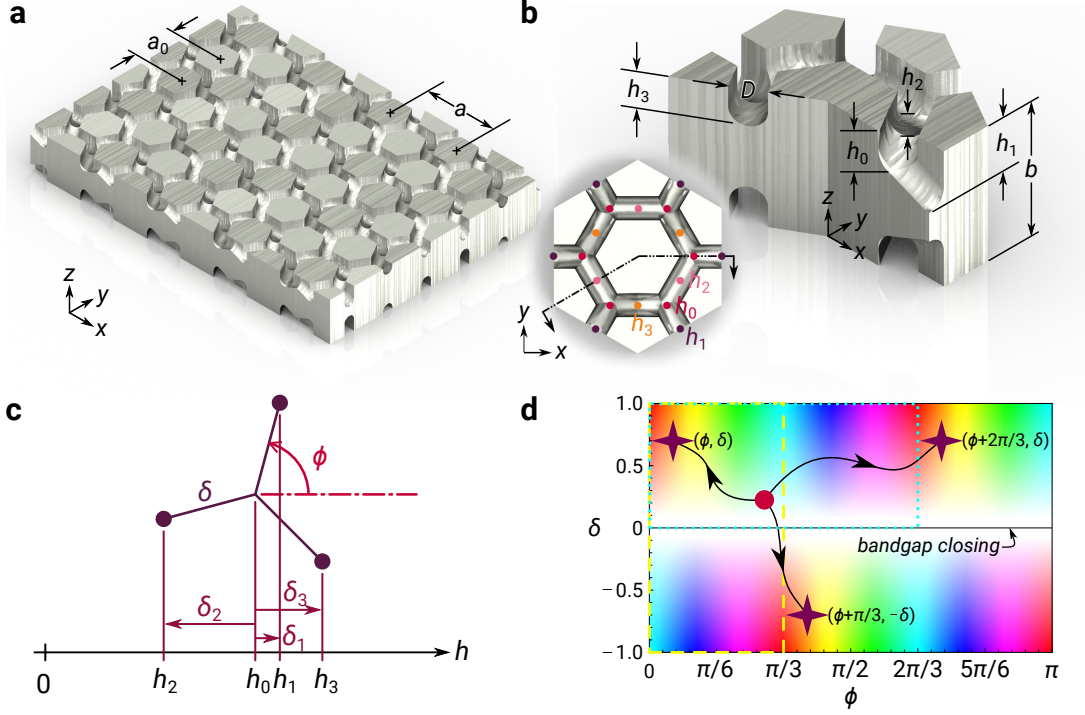


FIG. 2. (a) An illustration of the phononic elastic lattice consisting in an aluminum plate with a honeycomb-like groove pattern symmetrically engraved on both sides. Before application of the Kekulé distortion, the lattice has constant a_0 . After the distortion is applied, the lattice constant becomes $a = \sqrt{3}a_0$. (b) An isometric sectional view of a Wigner-Seitz unit cell of a distorted lattice centered at a C_3 axis. Three different depths $h_{1,2,3}$ are assigned to the midpoints of all the hexagon edges, and the average depth $h_0 = (h_1 + h_2 + h_3)/3$ is assigned at the vertices joining the edges. The grooves are constructed by linearly connecting neighboring grooves. The inset shows the top view of the unit cell. (c) A graphical representation showing the relation between the parameters (h_0, δ, ϕ) and (h_1, h_2, h_3) . (d) The parametric space to generate all admissible lattices. Different points with the same color yield the same bulk lattice pattern up to a rigid body translation (e.g., the three purple stars). Two examples of the irreducible parametric domains to generate a unique bulk lattice pattern are shown as the yellow dashed and the cyan dotted box. Depending on different paths, two distinct bulk lattice can evolve from one to another with or without band gap closing.

to a translation of the entire lattice by a vector $(0, -a_0)$ (see the inset in Fig. 2 (b)), or a counterclockwise rotation of $2\pi/3$ with respect to the point labeled h_0 along the z -axis in the inset of Fig. 2 (b). It follows that the parameter space in Fig. 2 (d) contains three copies of a certain subdomain that can generate the same bulk lattice. Two examples of the irreducible subdomain are highlighted by the yellow dashed and the cyan dotted boxes in 2 (d). One should find that (ϕ, δ) , $(\phi + \pi/3, -\delta)$ and $(\phi + 2\pi/3, \delta)$ yield the same bulk lattice up to a rigid rotation or translation, for all given (ϕ, δ) . Fig. 2 (d) shows all the possible bulk lattice patterns identified by colors. Specifically, the color reads (hue, lightness) = $(\frac{\phi}{3}, 1 - |\delta|)$ for $\delta \geq 0$ and $(\frac{\phi+\pi}{3}, 1 - |\delta|)$ for $\delta < 0$. For example, the three purple stars in Fig. 2 (d) mark points of the parameter space with the same color and, therefore, representing the same bulk lattice (up to a rigid translation). This consideration leads to a peculiar result that is, given a certain bulk lattice configuration (e.g. the red spot in Fig. 2 (d)), the lattice can evolve adiabatically into another (e.g. purple stars) by following several different paths in the parametric space that may or may not cross $\delta = 0$. As previously mentioned (and clarified in detail in the following), $\delta = 0$ identifies the closing of the bulk band gap. Considering that the closing and reopening of the band gap is an indicator

of a possible topological transition, the results in parameter space raises the interesting question as of if the two configurations belong to the same topological phase. A potentially even bolder statement could concern the two lattices belonging to the same bulk pattern and differing, at most, for a relative rigid translation (or rotation); could they be representing topologically distinct phases given that evolving from one to another can also induce the band gap to close and reopen? In case this latter question admitted a positive answer, then edge states might exist at a dislocation interface between these two phases. To gain more insight on this topic and answer the above question, the phononic band structure and its topological properties must be analyzed in detail.

III. PHONONIC BAND STRUCTURES AND TOPOLOGICAL BAND PROPERTIES

A. Band structure

Before introducing the Kekulé distortion (that is considering $(\delta = 0, h_1 = h_2 = h_3 = h_0)$), the “unit cell” in the inset of Fig. 2 (b) is a supercell, and its original primitive lattice is

characterized by basis lattice vectors having $1/\sqrt{3}$ length and rotated of $\pi/2$ with respect to those of the supercell. The band structure associated with this supercell exhibits a double Dirac cone at the Γ point (Fig. 3 (b)) that is the result of the folding of the two cones at the valleys $K_0(\frac{2\pi}{\sqrt{3}a_0}, \frac{-2\pi}{3a_0})$ and $K'_0(\frac{2\pi}{\sqrt{3}a_0}, \frac{2\pi}{3a_0})$ of the original primitive cell. This concept is visually exemplified in Fig. 3 (a) where the solid black hexagon indicates the first Brillouin zone (BZ) associated with the supercell and the black dashed hexagon shows the first BZ of the original primitive cell. The gray hexagons indicate the \mathbf{k} -space duplicates of the BZs. The original Dirac degeneracies at the valleys K_0 and K'_0 of the primitive cell were a consequence of intact space inversion symmetry (SIS) and TRS, while the new four-fold degeneracy at the Γ point of the supercell is an artifact of band folding and merely due to the artificial selection of supercell. However, the supercell could be taken as the new reference configuration (i.e. the primitive unit cell) when a local perturbation (such as the Kekulé distortion) is applied to it. The symmetry breaking resulting from the local perturbation would lift the four-fold degeneracy opening a band gap at the Γ point.

Figs. 3 (b) and (c) show the phononic band structures of the reference lattice ($\delta = 0$) and a distorted one ($\delta = 0.5, \phi = 0$), respectively. The band structure was obtained by numerically solving the elastodynamic governing equations for the Bloch eigenstates (computational details and band structures for other configurations are provided in Appendix ??). The black curves in the plots correspond to antisymmetric guided Lamb (A) modes, which are essentially flexural modes of the plate waveguide. The light gray curves show the symmetric (S) modes. Given the phononic plate is symmetric with respect to its neutral plane, the flexural modes are completely decoupled from the symmetric modes and from now on we will focus only on the flexural modes.

In Fig. 3 (b), the double Dirac cone with four-fold degeneracy shows at the Γ point, and the frequency bands are doubly degenerate throughout Γ -K. However, they split along the Γ -M direction. This is due to the anisotropy of the band structure near the valleys K_0 and K'_0 . Indeed, it is known that the dispersion around the valleys is only isotropic under linear \mathbf{k} approximation, and shows trigonal warping away from the valleys [38]. The two mirrored trigonally warped cones cross each other. The frequency spectra remain degenerate along the Γ -K section, corresponding to the original K_0 - K_0 and K'_0 - K'_0 directions (which happens to be the intersecting part of the two warped cones), while split along the Γ -M direction that corresponds to the original K_0 - Γ and K'_0 - K_0 directions. This already indicates a major discrepancy between the phononic “zone-folding” system and the electronic 2D topological insulators. For the latter, in the absence of inversion asymmetry, and spin-orbital coupling, the entire energy band structure are doubly degenerate. On the contrary, for phononic systems, the two-fold degeneracy only occurs along six discrete directions (Γ -K and Γ - K').

In Fig. 3 (c), under the effect of the Kekulé distortion, the four-fold degeneracy is lifted and a band gap opens up, as indicated by the pink shaded box. On the other hand, the spectra along Γ -K, are now lifted with the only exception of an isolated

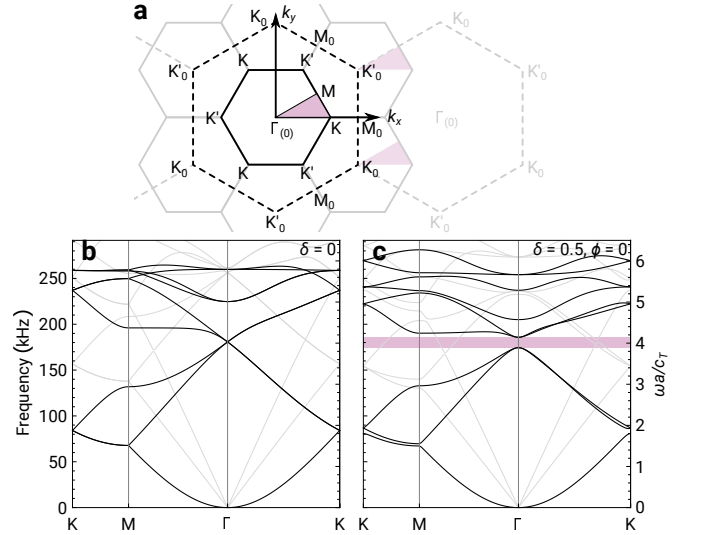


FIG. 3. (a) Schematic of the reciprocal space illustrating the formation of the double Dirac cone by zone folding. The solid black hexagon indicates the first Brillouin zone (BZ) associated with the supercell and the black dashed hexagon shows the first BZ related to the original primitive cell. The Dirac cones at the two valleys $K_0(\frac{2\pi}{\sqrt{3}a_0}, \frac{-2\pi}{3a_0})$ and $K'_0(\frac{2\pi}{\sqrt{3}a_0}, \frac{2\pi}{3a_0})$ of the primitive cell move to and overlap at the Γ point of the supercell. (b) The phononic band structures of the reference lattice ($\delta = 0$) and (c) of a Kekulé distorted lattice with $\delta = 0.5, \phi = 0$.

two-fold degeneracy at the Γ point. Although, up to this point, we have not provided a formal definition of the pseudospin, we anticipate that this behavior could be interpreted as an effective pseudospin-orbit coupling that splits the two pseudospin bands. We should also note that, in electronic systems, even in presence of spin-orbit coupling, the Kramers theorem requires that double degeneracies occur both at the Γ and the three M points (given that the M points are also invariant under $\mathbf{k} \rightarrow -\mathbf{k}$ as they are midpoints between two neighboring Γ points) [39]. Obviously the “zone-folding” system does not follow the same behavior, and shows significant splitting at the M point (Fig. 3 (b) and (c)). This again points out the discrepancy between the two systems.

In the literature, the standard procedure to analyze the system is through the $\mathbf{k} \cdot \mathbf{p}$ approach (or similar low-order perturbation approaches) which expands the eigenstates around the Γ point by using a basis formed by the degenerate eigenstates. This procedure leads to a description of the system in the form of a 4×4 block diagonal Hamiltonian that is quadratic in \mathbf{k} . After the application of a proper change in basis [22, 26], this Hamiltonian can be mapped to the Bernevig-Hughes-Zhang (BHZ) model of topological insulators. This simplified Hamiltonian yields four frequency bands that are quadratic in \mathbf{k} with the two upper and lower bands being doubly degenerate. The basis used to obtain this form of the Hamiltonian defines the pseudospin eigenstates.

Typically, the perturbed lattices are classified as “nontrivially” gapped materials if they satisfy the following conditions: 1) the spectra of the p - and d -orbitals are inverted [17], or 2)

$B/M < 0$ (where B and M are parameters from the BHZ Hamiltonian) [18]. However, it can be seen (see Appendix ??) that in a continuous and periodic medium, the parity of the wavefunctions used in classifying p - or d -orbitals depends on the reference frame. It is also reported that the mapping to the BHZ model actually depends on the gauge choice or the unit cell selection [22, 26], therefore the possible “nontrivial” character of the lattice is indeterminate. On the other hand, unlike nontrivial 2D topological insulators that support gapless helical edge states on the boundary, the phononic lattices classified as “nontrivial” still do not support edge states on its boundary with either vacuum or air. In these materials, edge states only exist on the interface between two gapped lattices. Therefore, the classification as a nontrivial material acquires a somewhat more arbitrary character and the conventional bulk-edge correspondence principle does not apply.

In addition, the low-order Hamiltonian cannot capture the band splitting along the Γ -M direction which is a distinctive feature compared with electronic systems. The band splitting of pseudospin pairs along the Γ -K direction occurs due to the higher order pseudospin-orbit coupling terms. These arguments show that the conventional perturbation approach is not sufficient for an accurate description of the phononic Kekulé lattice. In the following, we employ direct numerical calculations to define the pseudospins and further investigate the band structure and the corresponding topological properties.

B. Pseudospins

Unlike electrons having intrinsic spin states, the spin of the phonons can only be well-defined in isotropic media where the longitudinal phonon has spin 0 and the transverse one carries spin 1. In any crystal lattice, provided that the rotation symmetry is no longer a continuous group, purely longitudinal and transverse waves do not exist other than along prescribed directions. It follows that in a lattice, the phonon spin cannot be defined in a rigorous way, like the electron spin having discrete spin angular momentum [40].

As mentioned in the previous section, once the Kekulé distortion is introduced, the originally degenerate bands along Γ -K and Γ -K' directions are lifted. The resulting inversion asymmetry acts as a pseudomagnetic field and splits the pseudospin-pair bands, $\omega(\mathbf{k}, \uparrow) \neq \omega(\mathbf{k}, \downarrow)$. Direct observation of the eigenmodes obtained from the numerical results confirms that the eigenmodes of the two split bands have counter-rotating mechanical energy flux similar to the cyclotron motion of charged particles under magnetic field. We define the pseudospins directly using the sign of the pseudocyclotron frequency ω_z based on the mechanical energy flux circulation. Note that this definition based on direct numerical calculation can be applied to any eigenstate in the \mathbf{k} -space, and it is not restricted to doubly degenerate Γ -K or Γ -K' directions. The normalized pseudocyclotron frequency is defined as

$$\hat{\omega}_z = \frac{\omega_z}{\omega} = \frac{1}{\omega} \frac{L_z}{I_{zz}}, \quad (2)$$

where ω_z is the pseudocyclotron frequency given by L_z/I_{zz} ,

in which L_z and I_{zz} are the z -component of the pseudoangular momentum and the pseudomoment of inertia, respectively. These quantities are defined as

$$L_z = \int_{\text{cell}} d^3\mathbf{r} (\mathbf{r} \times \mathbf{J}) \cdot \hat{\mathbf{z}}, \quad (3)$$

$$I_{zz} = \int_{\text{cell}} d^3\mathbf{r} (\|\mathbf{r}\|^2 - z^2)w. \quad (4)$$

In the above expressions, $\mathbf{r} = (x, y, z)$ is the position vector with the origin of the coordinates located at the unit cell center, $\mathbf{J} = \frac{1}{2}\text{Re}(\boldsymbol{\sigma} \cdot \mathbf{v})$ is the period-averaged mechanical energy flux, while $\boldsymbol{\sigma}$ and \mathbf{v} are the stress tensor and the velocity vector, respectively. In Eq. 4, w is the period-averaged strain energy density reading $w = \frac{1}{4}\text{Re}(\boldsymbol{\sigma} \cdot \boldsymbol{\epsilon})$, and $\boldsymbol{\epsilon}$ is the strain tensor. Since the elastic wave is confined in a thin plate, we only consider the energy flux parallel to the xy -plane and the associated pseudoangular momentum with respect to the out-of-plane z -axis. Thus, the phonon pseudoangular momentum can only have the z -component; this is in contrast with the case of electrons that exhibit an internal spin angular momentum that can potentially point in any direction, even in 2D materials. We should also note that the definition we employ for the pseudoangular momentum is closer to the concept of orbital angular momentum rather than the internal spin angular momentum in the electron context.

Note that the pseudocyclotron frequency is introduced in order to facilitate the nondimensionalization process and it returns an average spinning frequency, meaning that it accounts for the energy flux of all pseudocyclotrons included in the integral domain. For simplicity, a Wigner-Seitz primitive cell centered at a C_3 symmetry axis (as shown in the inset Fig. 2 (b)) is chosen as the reference domain for integration. The ω - \mathbf{k} dispersion surfaces near the Γ point (0.08Γ -K) are plotted and color coded using $\hat{\omega}_z$. The results for three configurations identified by the parameters $\delta = 0.5$ and $\phi = [-2\pi/3, 0, 2\pi/3]$ are reported in Fig. 4 (a, b, c), respectively.

These plots can be leveraged to extract some useful information. First, we observe that in the presence of Kekulé distortion the frequency bands of the upper (lower) two neighboring bands are completely detached from each other except for an isolated degeneracy at the Γ point. The repulsion between the two upper (lower) bands, originally subject to trigonal warping, makes each of the four new bands acquire a hexagonal warping. Second, in Fig. 4 (a, c) it is found that the $\hat{\omega}_z$ pattern for each band shows a six-lobe alternating distribution, in which neighboring frequency bands exhibit opposite $\hat{\omega}_z$ values. The pseudoangular momentum has extreme values along the Γ -K and Γ -K' directions, where the spectrum was doubly degenerate before introducing the Kekulé distortion, and identically zero along the Γ -M directions, where the spectrum was split. From the pseudocyclotron frequency pattern, we define the pseudospins in the following way: pseudospin up (\uparrow) for parts of the frequency band with positive $\hat{\omega}_z$ values, and pseudospin down (\downarrow) for those with negative $\hat{\omega}_z$ values. Under such definition, a continuous band is not of a fixed pseudospin but has a six-lobe alternating pseudospin texture. On the other hand, a pseudospin “band” can be considered to be composed of parts from two neighboring independently con-

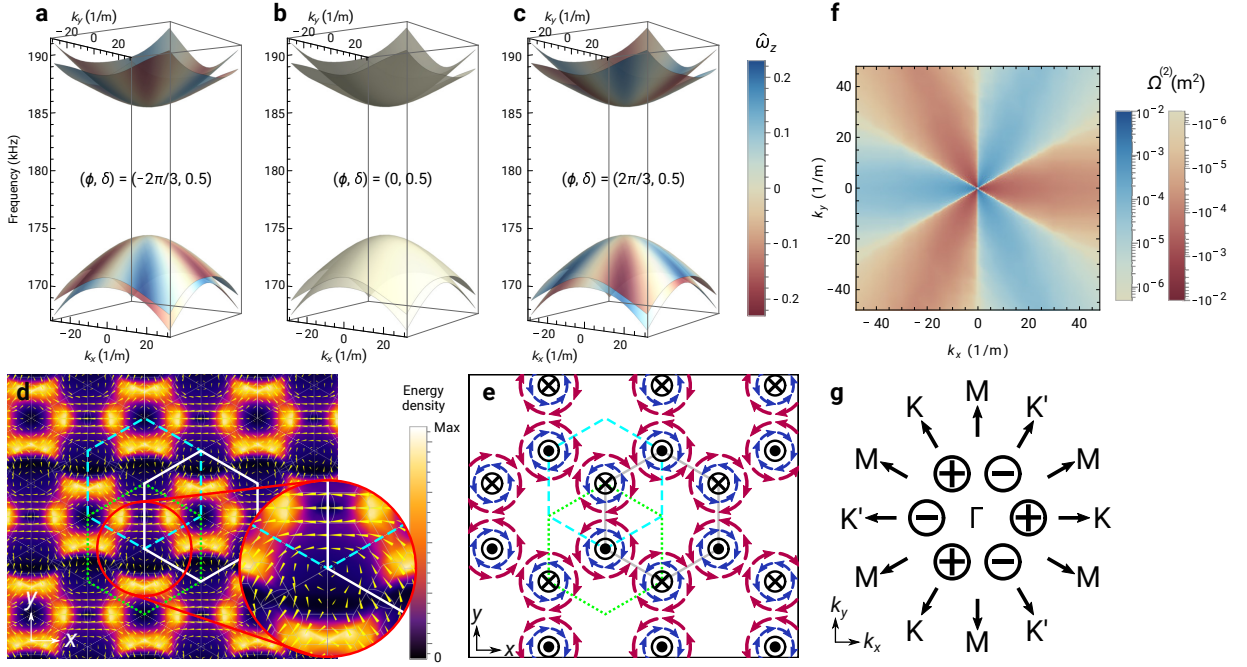


FIG. 4. (a-c) The ω - \mathbf{k} dispersion surfaces near the Γ point ($0.08 \Gamma\text{-K}$) for $\delta = 0.5$ and $\phi = -2\pi/3, 0, 2\pi/3$, respectively. The color marks the pseudocyclotron frequency (with the sign following right-hand rule). (d) Distribution of the strain energy density w along with the mechanical energy flux \mathbf{J} (yellow arrows in logarithmic scale), on the mid-plane of the phononic plate for a state on the second lowest band at $0.026 \Gamma\text{-K}$. The three hexagons with cyan dashed, white solid, and green dotted borders mark the Wigner-Seitz cells associated with (a-c), respectively. (e) Schematic showing the \mathbf{r} -dependence of the pseudomagnetic field. The cyan, green, and gray hexagons indicate the three possible choices of the Wigner-Seitz cells centered at a C_3 axis. The blue and red circulating arrows illustrate the pseudocyclotron motion of the eigenstate in the first and second lowest bands, respectively, assuming a \mathbf{k} point along $\Gamma\text{-K}$. The black in- and out-of-plane arrows show the \mathbf{r} -dependence of the pseudomagnetic field. (f) The Berry curvature Ω of the second lowest band in log scale. (g) The azimuth-angle-dependence of the pseudomagnetic field in the \mathbf{k} -space near the Γ point.

tinuous bands. From the above observations, it appears more obvious that the BHZ Hamiltonian based on two independent 2×2 massive Dirac Hamiltonian (one per each pseudospin) cannot describe completely our system and will not allow capturing possible geometric phases arising from the interaction between the pseudospin bands.

Another interesting observation concerns the cases $\phi = -2\pi/3, 0, 2\pi/3$. While, as previously mentioned, they represent the same bulk lattice up to a rigid-body translation, the corresponding pseudoangular momenta are found to be different. Indeed, they have the same magnitude but opposite signs for $\phi = \pm 2\pi/3$, and identically zero values for $\phi = 0$. To better illustrate such peculiarity, we plot the strain energy density w along with the mechanical energy flux \mathbf{J} (represented by yellow arrows) on the mid-plane of the phononic plate, as shown in Fig. 4 (d). The plot is taken at $(k_x, k_y) = (10, 0) \text{ m}^{-1}$ (along $0.026 \Gamma\text{-K}$) for the second lowest phononic band. The plot shows that in addition to an average leftward stream (associated with the negative x -gradient of the second lowest band at $0.026 \Gamma\text{-K}$), locally circulating patterns distribute repeatedly throughout the lattice. The three hexagons with cyan dashed, white solid, and green dotted borders mark the Wigner-Seitz cells (i.e., the domain of integration) for $\phi = -2\pi/3, 0, 2\pi/3$, respectively. The inset in Fig. 4 (d) shows a zoom-in near the center of the green hexagon to better visualize the direction of

the flux. Each of the three hexagons covers a full period of the pattern, but either opposite or net zero circulations about the centers are found. Since the reference frames and the location of each pseudocyclotron have no relative motion (i.e. they are fixed in physical space), the angular momentum of each pseudocyclotron should not vary with different reference frames. One may wonder if these results violate the parallel axis theorem of angular momentum? They do not. The reason is that the pseudocyclotron is periodically distributed, and for each hexagonal domain the integral takes into account portions from different pseudocyclotrons. Then, one may ask why not including all the pseudocyclotron contributions in the same integral domain? It turns out that the improper integral obtained by extending the integral domain in Eq. 3 to infinity does not converge; this is conceptually analogous to the divergent alternating series $\sum_{n=1}^{\infty} (-1)^n$ that oscillates endlessly. The previous discussion shows the intrinsic ambiguity in the pseudoangular momentum so that, for each band with a certain lattice momentum (k_x, k_y) , the pseudospin state is only determinate up to a specific choice of the reference frame.

In summary, in addition to the discrepancy in the band structure of the zone-folding system (compared with electronic QSH systems), the pseudospin indices are dependent on the observer and therefore ambiguous in their definition. In the result section, we will show that the pseudospin-dependent

Chern numbers are in fact gauge dependent. This latter statement might trigger an additional uncertainty and ambiguity in the possibility to define edge states. We will show that it is indeed because of this degree of indeterminacy, due to the dependence on the reference-frame, that we can conceive edge states along a dislocation boundary between two domains of the same bulk lattice.

C. Berry curvature and pseudomagnetic field

In the presence of the two-fold degeneracy at the Γ point for opposite pseudospin bands, a non-Abelian Berry phase is considered and the pseudospin-dependent Chern numbers form a 2×2 Chern number matrix (CNM) $C^{\alpha\beta} = \frac{1}{2\pi} \int d^2\mathbf{k} \Omega^{\alpha\beta}$, where $\alpha, \beta = \uparrow, \downarrow$ indicate the pseudospin index [41]. In the above, the overall integral of the inter-band Berry curvature $\Omega^{\alpha\beta}$, $\alpha \neq \beta$ yields zero, resulting in a diagonal CNM (see Appendix ?? for details). Therefore, in the following we will only focus on the diagonal elements of the Berry curvature matrix. Fig. 4 (f) shows the Berry curvature $\Omega^{(2)}$, where the superscript indicates the spectrum index (i.e. the Berry curvature of the second lowest band) in logarithmic scale. The Berry curvature is strongly localized around the Γ point at which becomes singular. Interestingly, it also exhibits a six-lobe alternating pattern with extreme values along Γ -K and Γ -K' and vanishing values along Γ -M directions; this pattern is similar to the one observed for the pseudocyclotron motion. However, differently from the pseudocyclotrons, the Berry curvature is a geometric property of the frequency band associated with the eigenstate evolution in \mathbf{k} -space, which is gauge invariant and does not vary with different reference frames. Such six-lobe pattern matches that obtained for the pseudospins; equivalently, $\Omega^{(2)}$ can be considered composed of $\Omega^{\uparrow\uparrow}$ and $\Omega^{\downarrow\downarrow}$, for each half of the BZ, as the blue and red parts shown in Fig. 4 (f), respectively. Similar considerations can be drawn for $\Omega^{(1)}$ by considering inverted pseudospin patterns. The Berry curvature is known as the \mathbf{k} -space magnetic field [42]. We find that this concept correlates well with the \mathbf{k} -space dependence of the pseudomagnetic field in the real \mathbf{r} -space that acts on the cyclotrons and splits the pseudospin frequency spectra. Figures 4 (e) and (g) show a schematic illustration of both the \mathbf{r} - and the \mathbf{k} -space dependence of the pseudomagnetic field $\mathbf{B}(\mathbf{k}, \mathbf{r})$.

In Fig. 4 (e), the three cyan, green, and gray hexagons again indicate the three possible choices (identical to those in Fig. 4 (d)) of the Wigner-Seitz cells centered at a C_3 axis. The red and blue circulating arrows illustrate the pseudocyclotron motion of the eigenstate in the first and second lowest bands (assuming a \mathbf{k} point along Γ -K), respectively. Given the known pseudocyclotron distribution, we can easily infer the inhomogeneous pseudomagnetic field \mathbf{B} , as depicted in black in- and out-of-plane arrows. The pseudomagnetic field must be parallel to the pseudomagnetic moment $\boldsymbol{\mu}$ of the pseudocyclotrons of the first band and antiparallel to that of the second band since the shifting of the frequency spectra is $-\boldsymbol{\mu} \cdot \mathbf{B}$ (assuming the pseudocyclotron carries positive “charge,” $\boldsymbol{\mu}$ can be inferred by the right-hand rule). We also note that, for each

pseudospin, the total flux through the unit cell is zero, which is analogous to the quantum Hall effect without Landau levels [43].

Similar to the electron systems, in the phononic pseudospin system the time-reversal partner of a certain eigenstate $|n(\mathbf{k}, \uparrow)\rangle$, is $|n(-\mathbf{k}, \downarrow)\rangle$ (except for the Γ -M directions where the spin vanishes). For example, the time-reversal partner of an eigenstate belonging to the second lowest band at some \mathbf{k} point along Γ -K, is the eigenstate at the $-\mathbf{k}$ point (along Γ -K') with opposite pseudospin. From the pseudospin pattern (Fig. 3 (a)), we know it is still on the second lowest band at the same frequency, which is also a direct result of TRS. It follows that the pseudospins flip, from momentum \mathbf{k} to $-\mathbf{k}$, and also for any $\pi/3$ change in the azimuth angle. Now, we can back up \mathbf{k} -dependence of the pseudomagnetic field that must switch signs for any $\pi/3$ change in the azimuth angle to yield the opposite spectra splitting for pseudospin-pair states, as shown in Fig. 4 (g). From the combination of Fig. 4 (e) and (g) we found the \mathbf{r} - and \mathbf{k} -dependence of the pseudomagnetic field in the current pseudospin Hall system, which is distinctive from the conventional Rashba-Dresselhaus effects [44].

D. Local topological order and bulk-edge correspondence

For electronic QSH systems, the \mathbb{Z}_2 topological order can be used to classify the nontrivial topological insulator phase from the ordinary one. The literature provides several different approaches to the calculation of the \mathbb{Z}_2 invariant [39, 41, 45, 46]. Examples include the use of the wavefunctions of the band pair at the four TR-invariant \mathbf{k} points (i.e., Γ and three M points, for triangular lattices) that bound half of the BZ [39], the integral of either the Berry connection or the Berry curvature in half of the BZ [45], and the difference in the Chern numbers of the opposite spin band in a pair [41], $\frac{1}{2} (C^{\uparrow\uparrow} - C^{\downarrow\downarrow}) \bmod 2$ for systems with spin conservation. The choice of a specific technique depends on specific symmetries available for the system, as well as on the availability of the Hamiltonian or the band structure.

For the current “zone-folding” system, given there is no Kramers degeneracy at the M point as we have seen in Fig. 3, we cannot make use of the wavefunctions to find \mathbb{Z}_2 . In fact, we can only focus on the vicinity of the Γ point to define a local topological order that resemble the \mathbb{Z}_2 invariant.

Similarly to elastic valley Hall systems [35], in which the resulting valley dependent Chern numbers are $\pm 1/2$, also in the current system the pseudospin dependent Chern number is half-quantized $C^{\uparrow\uparrow/\downarrow\downarrow} = \pm 1/2$ or $\mp 1/2$, where \pm or \mp depends on the choice of the unit cell. This is clearly a direct consequence of the folding which brings the valleys of the initial cell to coincide at the Γ point of the distorted cell. We can therefore define a local topological order, which conceptually follows the same principle of a \mathbb{Z}_2 invariant, in the form $\nu = \frac{1}{2} (C^{\uparrow\uparrow} - C^{\downarrow\downarrow})$.

Since the two pseudospin dependent Chern numbers have opposite signs ($\pm 1/2$) and switch signs simultaneously under different reference frames, the evaluated local topological order of a specific lattice can be either $\nu = +1/2$ or $-1/2$,

depending on the choice of reference frames. These fractional and gauge dependent values indicate that the defined local topological order is not an exact topological invariant as it is obtained from local integral of Berry curvature which does not cover the entire effective Brillouin zone [46]. In fact, in the “zone-folding” system, we cannot have any topological phase transition in a strict sense as one can easily see from Fig. 2 (d) in which a path connecting any two distinct bulk lattices configurations that do not cross the abscissa $\delta = 0$ can always be found. In other terms, any two bulk lattices can evolve adiabatically from one to the other without closing the band gap; hence the exact topological invariant does not change.

However, the local topological order appears to be a useful indicator to predict the number of Kramers pair edge states on an interface $N_K = \Delta\nu \bmod 2$ [1], where $\Delta\nu$ is the change in the local topological order across the interface. As an example, similarly to electronic topological insulators in which a pair of edge states can exist on its outer boundary (i.e., interface between the nontrivial QSH material, $\mathbb{Z}_2 = 1$, and vacuum, $\mathbb{Z}_2 = 0$), in the “zone-folding” system a pair of band-gap-crossing edge states can be synthesised on an interface connecting two materials with $\nu_1 = +1/2$ and $\nu_2 = -1/2$.

Given that the sign of the local topological order ν depends on the choice of the reference frame, it is natural to wonder if an edge state can exist on the interface between lattices having the same bulk pattern but differing up to a relative translation (i.e., a dislocation interface). Numerical and experimental results in the following sections show that these edge states are indeed possible. The following section provides a way to conceive a pair of gapless pseudospin-polarized edge states on a dislocation interface.

IV. HELICAL EDGE STATES ON A DISLOCATION INTERFACE

Electronic topological insulators have two *helical* edge states that are topologically protected, counter-propagating, and with gapless energy spectra across the entire band gap. The gapless condition at the high symmetry points in \mathbf{k} -space ($k_{\parallel} = 0, \pm\pi/a$ along the edge) is guaranteed by Kramers theorem under TRS, $E(\mathbf{k}, \uparrow) = E(-\mathbf{k}, \downarrow)$. On the other hand, the existing literature shows that, in a phononic analog of a topological insulator based on the zone-folding approach, the edge states are generally gapped at $k_{\parallel} = 0$. This result is due to the fact that Kramers theorem is valid only for systems with half-integer total spin, such as electronic systems. In the phononic systems, the “synthetic Kramers pair” is created by the pseudospins. When the two pseudospin states are close, in \mathbf{k} -space, they tend to repel each other and the eigenstates show strong mixing that completely annihilates the pseudospins. Given that the pseudospin is generally not conserved, the Kramers degeneracy does not hold and the gap at $k_{\parallel} = 0$ typically appears for the phononic edge states. This observation also means that the edge states are not robust and prone to backscattering since the counter-propagating edge states are already strongly coupled and gapped even before introducing defects. Previous studies ascribed the presence of the gap to the lack of C_{6v} symmetry of

the lattice near the domain wall interface [17], and attempted to reduce the gap width by smoothing the transition between the two lattices [20]. However, as we will show later, the gapless edge state actually does not require local C_{6v} symmetry and can exist on an abrupt dislocation interface.

Given the pseudocyclotrons have a certain distributed pattern throughout the phononic lattice, the position of the edge which terminates the bulk lattice (or equivalently, the translation of the bulk pattern relative to the edge) is certainly expected to serve as a key parameter and to affect the behavior of the edge state propagating on it. A proper skipping-orbit condition on the edge can in fact realize nonrestrictive ballistic transport of the phonons and therefore, achieving fully decoupled, counter-propagating, and gapless phononic helical edge states. In a recent study [26], it was shown that this condition can be realized by fine-tuning the parameter ϕ of the two adjacent lattices that are space-inverted images of each other. In this study, in order to demonstrate that the edge state can exist on a dislocation interface, we let the adjacent lattices have the same bulk lattice pattern so that they can differ only up to a relative translation of amplitude a_0 along the y -direction. Such translation distance preserves the overall honeycomb pattern across the two lattices which, although not necessary, makes the fabrication of the material sample easier. Under a fixed reference frame, this lattice assembly can be also considered as integrating two lattices with parameters ϕ and $\phi + 2\pi/3$. To make it even simpler, we let $\phi = 0$, so that the dislocation interface is a plane of mirror symmetry. Once again, these assumptions do not limit the generality of the results and facilitate the final lattice configuration used for the experiment. Indeed, under these conditions, the edge state will be symmetric with respect to the interface, hence facilitating its excitation via a single transducer placed right on the interface.

By modifying the depth of the groove located on the interface, the edge state dispersion can be readily tuned. In particular, by sweeping through different depths, we find the value such that the edge states reaches accidental degeneracy at $k_{\parallel} = 0$ (see Appendix ?? for details). Fig. 5 (a) shows the edge state spectrum along the optimized dislocation interface, and Fig. 5 (b) shows the strain energy distribution and the mechanical energy flux of the eigenstate indicated by the arrow in Fig. 5 (a). The color in Fig. 5 (a) denotes the pseudoangular momentum of each eigenstate, whose integral is calculated over a complete hexagonal cell located just next to the dislocation, as shown in the dashed cyan hexagon in Fig. 5 (b). These results also show that the two edge states are indeed pseudospin polarized, fully decoupled, counter-propagating and gapless, therefore a successful synthetic Kramers pair. The mechanical energy flux near the symmetric dislocation interface in Fig. 5 (b) also indicates a typical skipping-orbit pattern. Note that the edge state is achieved on an abrupt dislocation, that is without a transition zone smoothing the change in lattice patterns; in addition, the unit cells on the dislocation does not possess C_{6v} symmetry.

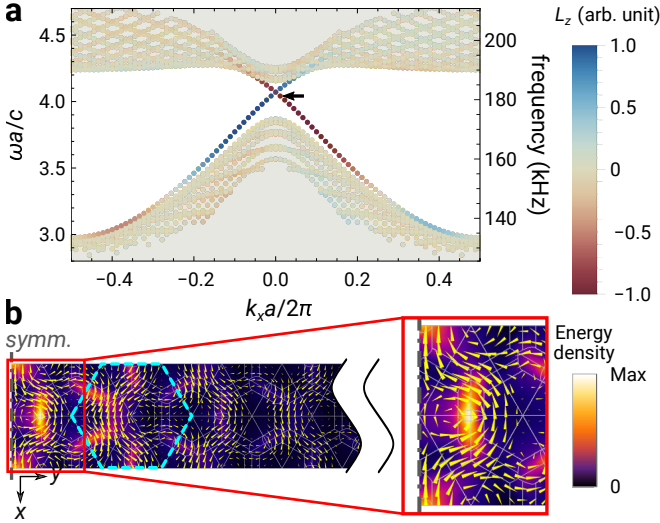


FIG. 5. (a) The edge state spectrum along the optimized dislocation interface. The color denotes the pseudoangular momentum. (b) The strain energy distribution (color) and the mechanical energy flux (yellow arrow, log scale) of the eigenstate indicated by the arrow in (a). The dashed cyan hexagon shows the domain used for the pseudoangular momentum integral. The energy flux near the interface indicates a typical skipping-orbit pattern.

V. EXPERIMENTS

In order to experimentally validate this concept of topological elastic material, we fabricated the phononic plate having two subdomains made of the same bulk honeycomb pattern but differing up to a relative translation. The two domains were used to define a Z-shape dislocation interface (Fig. 6) similarly to the example illustrated in the previous section. Further details on the fabrication and the experimental setup are provided in the Appendix ??). Two piezoelectric ceramic plates were glued at the top terminal of the Z-dislocation, on both sides of the plate, as shown in Fig. 6 (a, b). The red arrows in Fig. 6 (b) indicate the poling direction of the piezoelectric ceramic plates. They align in the same $+z$ -direction and act out-of-phase when applying the voltage on their outer electrodes. This configurations helps triggering primarily the A_0 mode. The response of the plate in terms of the velocity field distribution was measured by a scanning laser Doppler vibrometer.

Figure 6 (c) shows the measured velocity amplitude at 172 kHz, which indicates the edge state propagating along the Z-dislocation. To obtain the edge state dispersion from the measured data, data points along the first segment of the Z-dislocation (enclosed in the white box in Fig. 6 (c)) were selected and Fourier transformed so to obtain the k_{\parallel} -spectra (in the range 150-200 kHz) shown in Fig. 6 (d). The calculated pseudospin-up edge state (cyan dashed curves) and the bulk band dispersion curves (white dotted curve), previously shown in Fig. 5(a), are superimposed on the spectrum. The curves were down shifted by 7 kHz (fractional shift of -3.8% , normalized by the calculated edge state center frequency) to align with the experiment data. This is a small error consider-

ing the operating frequency range and it is likely due to slight deviations of the mechanical properties of the aluminum alloy from the nominal values as well as to small fabrication imperfections. Nevertheless, results confirm that the edge state along the dislocation is indeed gapless across the bulk band gap and that there is no evidence of coupling to the counter-propagating edge state in the presence of sharp corners on the path.

The weak attenuation visible along the consecutive sections is likely the result of a few factors. a) There is energy accumulation on the top edge due to the limited absorbing performance of the viscoelastic layer. This accumulation acts as an incoherent source of energy that feeds back into the channel. After this incoherent component of the input is reflected at the first corner, the two remaining branches appear markedly more uniform. b) The measured response contains not only the edge state, but also the evanescent bulk wave in the band gap. The response of the latter decays exponentially (anisotropically) from the transducers, therefore the mixed response shows larger amplitude on the first section. c) The decay of the edge state is partially due to the asymmetry of the phononic plate. In Appendix ?? we describe the uneven machining result on the two sides which leads to slight asymmetry with respect to the mid-plane. The asymmetry caused weak coupling between antisymmetric and symmetric modes. The continuous spectrum of the symmetric modes in the bulk band gap of the antisymmetric modes leads to the energy leakage into bulk symmetric modes in the presence of coupling between A and S modes.

We also conducted a time-transient measurement using a wave packet centered at 172 kHz as the input signal shown in Fig. 7 (a). Instantaneous velocity profiles at selected time frames are shown in Fig. 7 (b-i). Results evidently show that the wave packet propagate through the two acute corners without observable reflections. The faster wave with longer wavelength visible in early frames (b-d) is the symmetric bulk mode triggered during the ramp up phase of the transient. A full video of the transient response is also provided in the Supplemental Material [47].

VI. SUMMARY

This study presented a fully continuous 2D elastic topological waveguide based on the concept of a Kekulé distorted lattice and capable of truly gapless phononic edge states. A combination of theoretical and numerical results showed that this phononic pseudospin Hall system cannot be studied and entirely understood by means of traditional perturbation techniques. Reverting to an approach based on in-depth numerical simulations allowed us to show a discrepancy of the degenerate band structure of “zone-folding” systems compared to electronic quantum spin Hall systems. This approach also yielded the fine structure of the spectrum splitting due to pseudospin-orbit coupling caused by inversion asymmetry, also not observable via standard perturbation techniques. We introduce a definition of the pseudospin that allows all eigenstates in \mathbf{k} -space to be labeled clearly and that ultimately reveals a

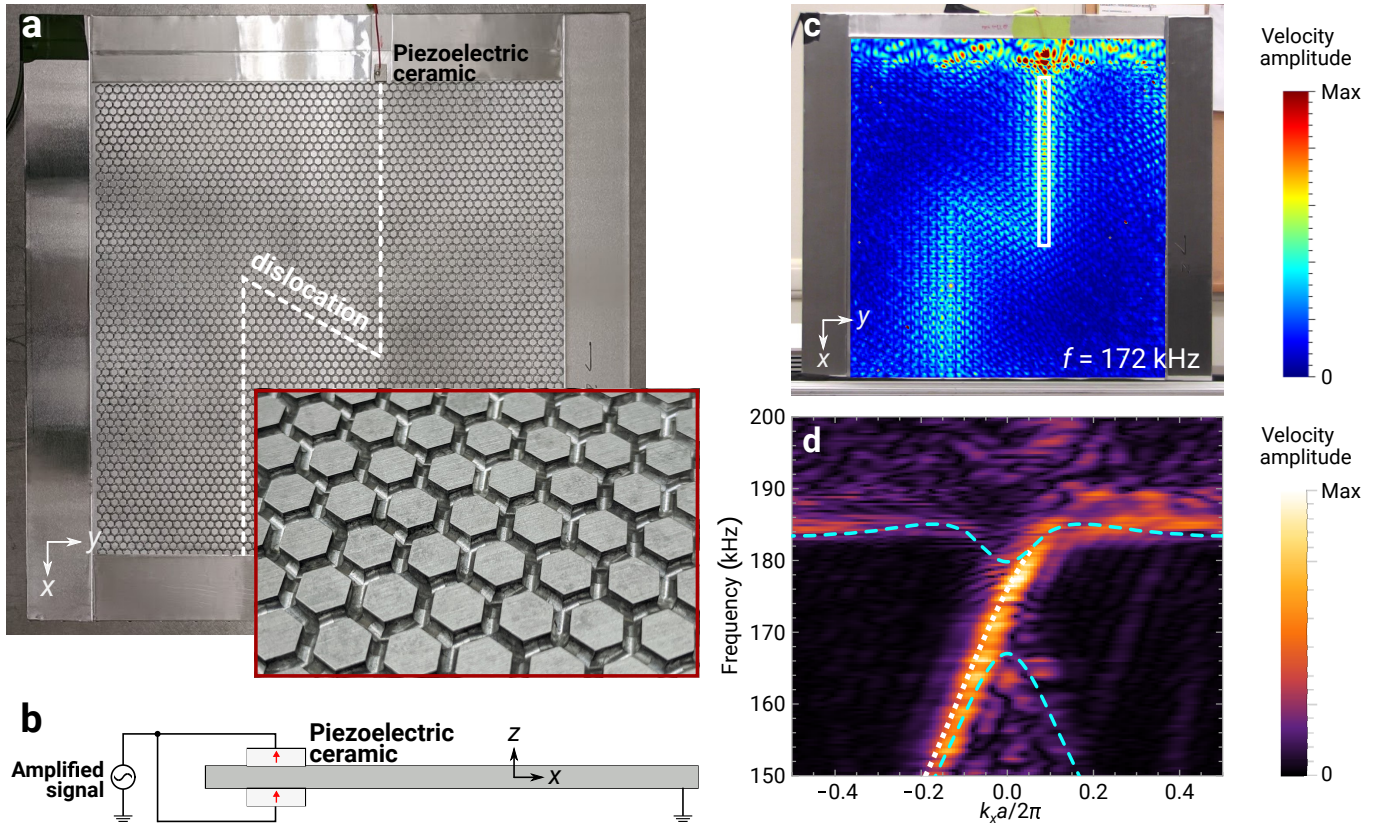


FIG. 6. (a) An image of the fabricated phononic plate. The Z-shape dislocation interface between the two subdomains is indicated by the white dashed line. Piezoelectric ceramic transducers were glued at the top terminal of the Z-dislocation and on both sides of the plate, in order to generate A_0 Lamb waves. (b) An illustration of the transducer system and its connections. The red arrows indicate the poling direction of the piezoelectric ceramic plates. (c) The measured velocity amplitude at 172 kHz. The white dashed box includes the data points selected for 1D Fourier transform. (d) The k_x -spectra in the range 150-200 kHz. The calculated pseudospin-up edge state (cyan dashed curves) and bulk band (white dotted curve) dispersion curves are superimposed to the experimental results. The curves were down shifted by 7 kHz (fractional shift of -3.8%) to match with the experiment data. Results confirm that the edge state along the dislocation is indeed gapless and there is no evidence of coupling to the counter-propagating edge state due to the presence of sharp corners on the path.

distinctive alternating six-lobe pseudospin texture. By direct observation of the eigenstates, we also isolate the origin of the ambiguity of the pseudospin state, and constructed the \mathbf{r} - and \mathbf{k} -dependence of the pseudomagnetic field associated with the symmetry breaking. The ambiguity in the pseudospin state also leads to indeterminate pseudospin dependent Chern numbers. We find that the Kekulé lattices have the local topological order $\nu = \pm 1/2$ which leads us to affirm that the existence of edge states. While phononic gapless edge states at zero momentum had not been observed previously, we showed numerical and experimental evidence of their existence in our elastic phononic system. More specifically, edge states were found to be able to propagate on a dislocation interface of two adjacent identical bulk lattices differing only up to a relative translation. The robustness of these states was examined by propagating elastic wave packets into the dislocation waveguide with no observable backscattering at sharp corners along the path. The experimental results were fully consistent with the dispersion structure predicting gapless edge states

and decoupled pseudospin polarizations, therefore suggesting that the two counter-propagating edge states form a successful synthetic Kramers pair.

The approach presented in this study suggests a simple yet robust approach to turn any elastic plate structure into a topological waveguide capable of backscattering protected states while still preserving its structural properties. The possibility of creating such highly controlled states on simple dislocations also greatly simplify both design and fabrication. It is possible to envision the application of this concept to customize the dynamic response of thin wall structures in the context of, as an example, vibration and structure-born noise control, acoustic signal transmission, analog wave filtering.

ACKNOWLEDGMENTS

The authors thankfully acknowledge the financial support from the National Science Foundation under grant #1761423.

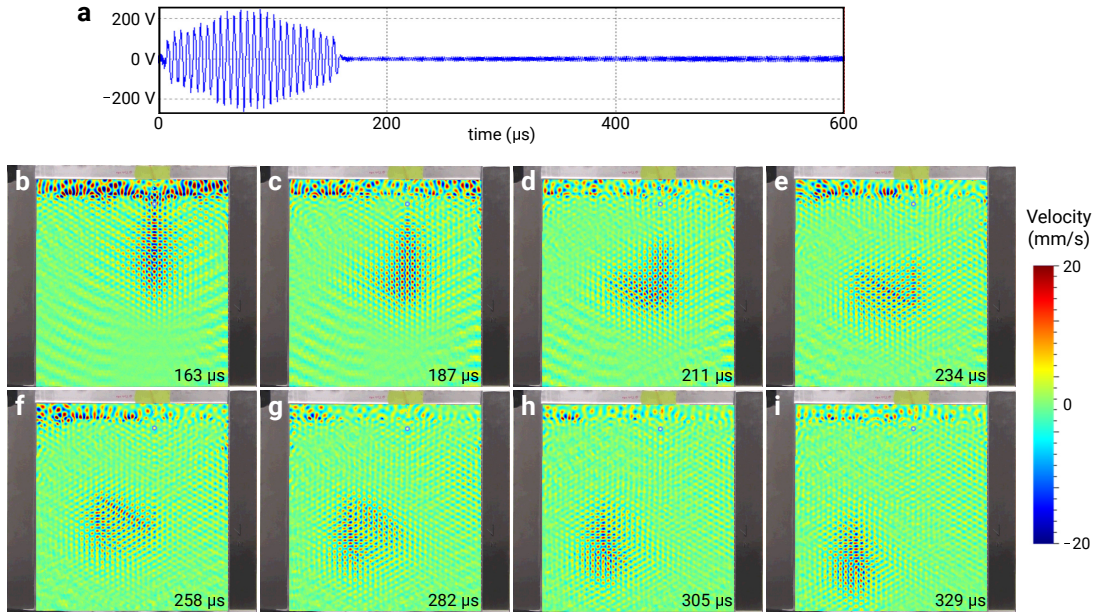


FIG. 7. The response of the phononic plate to a transient excitation. (a) The wave packet used as input signal. (b-i) Instantaneous velocity profiles at selected time frames. The wave packet can travel undisturbed through the two acute corners without observable reflections.

-
- [1] M. Z. Hasan and C. L. Kane, Colloquium: Topological insulators, *Rev. Mod. Phys.* **82**, 3045 (2010).
 - [2] Y. Ren, Z. Qiao, and Q. Niu, Topological phases in two-dimensional materials: a review, *Rep. Prog. Phys.* **79**, 066501 (2016).
 - [3] X.-L. Qi and S.-C. Zhang, Topological insulators and superconductors, *Reviews of Modern Physics* **83**, 1057 (2011).
 - [4] L. Lu, J. D. Joannopoulos, and M. Soljačić, Topological photonics, *Nat. Photon.* **8**, 821 (2014).
 - [5] T. Ozawa, H. M. Price, A. Amo, N. Goldman, M. Hafezi, L. Lu, M. C. Rechtsman, D. Schuster, J. Simon, O. Zilberberg, and I. Carusotto, Topological photonics, *Rev. Mod. Phys.* **91**, 015006 (2019).
 - [6] A. B. Khanikaev and G. Shvets, Two-dimensional topological photonics, *Nature photonics* **11**, 763 (2017).
 - [7] X. Zhang, M. Xiao, Y. Cheng, M.-H. Lu, and J. Christensen, Topological sound, *Communications Physics* **1**, 1 (2018).
 - [8] G. Ma, M. Xiao, and C. T. Chan, Topological phases in acoustic and mechanical systems, *Nature Reviews Physics* **1**, 281 (2019).
 - [9] F. Haldane and S. Raghu, Possible realization of directional optical waveguides in photonic crystals with broken time-reversal symmetry, *Physical review letters* **100**, 013904 (2008).
 - [10] Z. Wang, Y. Chong, J. D. Joannopoulos, and M. Soljačić, Reflection-free one-way edge modes in a gyromagnetic photonic crystal, *Physical review letters* **100**, 013905 (2008).
 - [11] X. Ni, D. Putseladze, D. A. Smirnova, A. Slobzhanyuk, A. Alù, and A. B. Khanikaev, Spin-and valley-polarized one-way klein tunneling in photonic topological insulators, *Science advances* **4**, eaap8802 (2018).
 - [12] L. M. Nasha, D. Kleckner, A. Read, V. Vitell, A. M. Turner, and W. T. M. Irvine, Topological mechanics of gyroscopic metamaterials, *Proc. Natl. Acad. Sci. U.S.A.* **112**, 14495 (2015).
 - [13] Z.-G. Chen and Y. Wu, Tunable topological phononic crystals, *Phys. Rev. Appl.* **5**, 054021 (2016).
 - [14] A. B. Khanikaev, R. Fleury, S. H. Mousavi, and A. Alu, Topologically robust sound propagation in an angular-momentum-biased graphene-like resonator lattice, *Nat. Comms.* **6**, 8260 (2015).
 - [15] P. Wang, L. Lu, and K. Bertoldi, Topological phononic crystals with one-way elastic edge waves, *Phys. Rev. Lett.* **115**, 104302 (2015).
 - [16] Z. Yang, F. Gao, X. Shi, X. Lin, Z. Gao, Y. Chong, and B. Zhang, Topological acoustics, *Phys. Rev. Lett.* **114**, 114301 (2015).
 - [17] L.-H. Wu and X. Hu, Scheme for achieving a topological photonic crystal by using dielectric material, *Physical review letters* **114**, 223901 (2015).
 - [18] C. He, X. Ni, H. Ge, X.-C. Sun, Y.-B. Chen, M.-H. Lu, X.-P. Liu, and Y.-F. Chen, Acoustic topological insulator and robust one-way sound transport, *Nat. Phys.* **12**, 1124 (2016).
 - [19] Y. Deng, H. Ge, Y. Tian, M. Lu, and Y. Jing, Observation of zone folding induced acoustic topological insulators and the role of spin-mixing defects, *Phys. Rev. B* **96**, 184305 (2017).
 - [20] R. Chaunsali, C.-W. Chen, and J. Yang, Subwavelength and directional control of flexural waves in zone-folding induced topological plates, *Phys. Rev. B* **97**, 054307 (2018).
 - [21] R. Chaunsali, C.-W. Chen, and J. Yang, Experimental demonstration of topological waveguiding in elastic plates with local resonators, *New Journal of Physics* **20**, 113036 (2018).
 - [22] Y. Liu, C.-S. Lian, Y. Li, Y. Xu, and W. Duan, Pseudospins and topological effects of phonons in a kekulé lattice, *Physical review letters* **119**, 255901 (2017).
 - [23] Y. Yang, Y. F. Xu, T. Xu, H.-X. Wang, J.-H. Jiang, X. Hu, and Z. H. Hang, Visualization of a unidirectional electromagnetic waveguide using topological photonic crystals made of dielectric materials, *Physical review letters* **120**, 217401 (2018).
 - [24] S.-Y. Yu, C. He, Z. Wang, F.-K. Liu, X.-C. Sun, Z. Li, H.-Z. Lu, M.-H. Lu, X.-P. Liu, and Y.-F. Chen, Elastic pseudospin transport for integratable topological phononic circuits, *Nature communications* **9**, 1 (2018).

- [25] Y. Zhou, P. R. Bandaru, and D. F. Sievenpiper, Quantum-spin-hall topological insulator in a spring-mass system, *New Journal of Physics* **20**, 123011 (2018).
- [26] T.-W. Liu and F. Semperlotti, Nonconventional topological band properties and gapless helical edge states in elastic phononic waveguides with kekulé distortion, *Phys. Rev. B* **100**, 214110 (2019).
- [27] Y. Deng, M. Lu, and Y. Jing, A comparison study between acoustic topological states based on valley hall and quantum spin hall effects, *The Journal of the Acoustical Society of America* **146**, 721 (2019).
- [28] C. Brendel, V. Peano, O. Painter, and F. Marquardt, Snowflake phononic topological insulator at the nanoscale, *Phys. Rev. B* **97**, 020102 (2018).
- [29] S. H. Mousavi, A. B. Khanikaev, and Z. Wang, Topologically protected elastic waves in phononic metamaterials, *Nat. Commun.* **6**, 8682 (2015).
- [30] M. Miniaci, R. Pal, B. Morvan, and M. Ruzzene, Experimental observation of topologically protected helical edge modes in patterned elastic plates, *Physical Review X* **8**, 031074 (2018).
- [31] J. Lu, C. Qiu, L. Ye, X. Fan, M. Ke, F. Zhang, and Z. Liu, Observation of topological valley transport of sound in sonic crystals, *Nat. Phys.* **13**, 369 (2016).
- [32] R. K. Pal and M. Ruzzene, Edge waves in plates with resonators: an elastic analogue of the quantum valley hall effect, *New Journal of Physics* **19**, 025001 (2017).
- [33] J. Vila, R. K. Pal, and M. Ruzzene, Observation of topological valley modes in an elastic hexagonal lattice, *Phys. Rev. B* **96**, 134307 (2017).
- [34] Y. Kang, X. Ni, X. Cheng, A. B. Khanikaev, and A. Z. Genack, Pseudo-spin-valley coupled edge states in a photonic topological insulator, *Nature communications* **9**, 1 (2018).
- [35] T.-W. Liu and F. Semperlotti, Tunable acoustic valley-hall edge states in reconfigurable phononic elastic waveguides, *Physical Review Applied* **9**, 014001 (2018).
- [36] H. Zhu, T.-W. Liu, and F. Semperlotti, Design and experimental observation of valley-hall edge states in diatomic-graphene-like elastic waveguides, *Phys. Rev. B* **97**, 174301 (2018).
- [37] T.-W. Liu and F. Semperlotti, Experimental evidence of robust acoustic valley hall edge states in a nonresonant topological elastic waveguide, *Physical Review Applied* **11**, 014040 (2019).
- [38] R. Saito, G. Dresselhaus, and M. Dresselhaus, Trigonal warping effect of carbon nanotubes, *Physical Review B* **61**, 2981 (2000).
- [39] C. L. Kane and E. J. Mele, Z₂ topological order and the quantum spin hall effect, *Phys. Rev. Lett.* **95**, 146802 (2005).
- [40] A. Levine, A note concerning the spin of the phonon, *Nuovo Cimento* **26** (1962).
- [41] D. N. Sheng, Z. Y. Weng, L. Sheng, and F. D. M. Haldane, Quantum spin-hall effect and topologically invariant chern numbers, *Phys. Rev. Lett.* **97**, 036808 (2006).
- [42] M. V. Berry, Quantal phase factors accompanying adiabatic changes, *Proceedings of the Royal Society of London. A. Mathematical and Physical Sciences* **392**, 45 (1984).
- [43] F. D. M. Haldane, Model for a quantum hall effect without landau levels: Condensed-matter realization of the "parity anomaly", *Phys. Rev. Lett.* **61**, 2015 (1988).
- [44] L. Meier, G. Salis, I. Shorubalko, E. Gini, S. Schön, and K. Ensslin, Measurement of rashba and dresselhaus spin-orbit magnetic fields, *Nature Physics* **3**, 650 (2007).
- [45] L. Fu and C. L. Kane, Time reversal polarization and a z₂ adiabatic spin pump, *Physical Review B* **74**, 195312 (2006).
- [46] J. E. Moore and L. Balents, Topological invariants of time-reversal-invariant band structures, *Physical Review B* **75**, 121306 (2007).
- [47] See Supplemental Material for the video of the measured transient edge state response.